Journal of Nuclear Medicine, published on May 7, 2015 as doi:10.2967/jnumed.114.153338

ImmunoPET of murine T cell reconstitution post-adoptive stem cell transplant using anti-CD4 and anti-CD8 cys-diabodies

Richard Tavaré,[1*] Melissa N. McCracken,[2] Kirstin A. Zettlitz,[1] Felix B. Salazar,[1] Tove Olafsen,[1] Owen N. Witte,[2-5] and Anna M. Wu[1*]

[1]Crump Institute for Molecular Imaging, Department of Molecular and Medical Pharmacology, David Geffen School of Medicine at University of California Los Angeles (UCLA), Los Angeles, CA, USA; [2]Department of Molecular and Medical Pharmacology, David Geffen School of Medicine at UCLA, Los Angeles, CA, USA; [3]Howard Hughes Medical Institute at UCLA, Los Angeles, CA, USA; [4]Department of Microbiology, Immunology and Molecular Genetics at UCLA, Los Angeles, CA, USA; [5]Eli and Edythe Broad Center of Regenerative Medicine and Stem Cell Research at UCLA, Los Angeles, CA, USA

[*]**Corresponding Authors**: Richard Tavaré, PhD, California NanoSystems Institute 4350B, University of California, Los Angeles, 570 Westwood Plaza, Los Angeles, CA 90095-1770, Tel: 310-267-2819, Fax: 310-206-8975, email: rtavare@mednet.ucla.edu. Anna M. Wu, PhD, California NanoSystems Institute 4335, University of California, Los Angeles, 570 Westwood Plaza, Los Angeles, CA 90095-1770, Tel: 310-794-5088, Fax: 310-206-8975, email: awu@mednet.ucla.edu.

Word Count: 4908

Disclosures: Anna M. Wu has ownership interest in and is a consultant/advisory board member for ImaginAb, Inc. Richard Tavaré is a consultant to ImaginAb, Inc. Tove Olafsen was a consultant to ImaginAb, Inc. at the time the research was performed and is currently an employee of ImaginAb, Inc. Part of the technology described in this manuscript is licensed by the Regents of the University of California to ImaginAb, Inc and the Regents have taken equity in ImaginAb, Inc as part of the licensing transaction.

Financial Support: This work was supported by the UCLA Scholars in Oncologic Molecular Imaging training program [National Institutes of Health (NIH) R25T CA098010], NIH grants R21 AI114255 and R21 CA190044, and by the California Institute for Regenerative Medicine (CIRM; RT1-01126-1). M.N.M. is supported by the CIRM Training Grant TG2-01169 and the UCLA In vivo Cellular and Molecular Imaging Center Career Development Award P50 CA086306. O.N.W. is an investigator of the Howard Hughes Medical Institute and is partially supported by the Eli and Edythe Broad Center of Regenerative Medicine and Stem Cell Research. Small animal imaging studies were supported by the UCLA Jonsson Comprehensive Cancer Center (NIH CA016042).

Running title: ImmunoPET of $CD4^+$ and $CD8^+$ T cell reconstitution

ABSTRACT

The proliferation and trafficking of T lymphocytes in immune responses are crucial events in determining inflammatory responses. To study whole body T lymphocyte dynamics non-invasively in vivo, we have generated anti-CD4 and -CD8 cys-diabodies (cDbs) derived from the parental antibody hybridomas GK1.5 and 2.43, respectively, for ^{89}Zr-immunoPET detection of helper and cytotoxic T cell populations.

Methods: Anti-CD4 and -CD8 cys-diabodies were engineered, produced via mammalian expression, purified using immobilized metal affinity chromatography, and characterized for T cell binding. The cys-diabodies were site-specifically conjugated to maleimide-desferrioxamine for ^{89}Zr radiolabeling and subsequent microPET/CT acquisition and ex vivo biodistribution in both wild type mice and a model of hematopoietic stem cell (HSC) transplantation.

Results: ImmunoPET and biodistribution studies demonstrate targeting and visualization of CD4 and CD8 T cell populations in vivo in the spleen and lymph nodes of wild type mice, with specificity confirmed through in vivo blocking and depletion studies. Subsequently, a murine model of HSC transplantation demonstrated successful in vivo detection of T cell repopulation at 2, 4, and 8 weeks post-HSC transplant using the ^{89}Zr-radiolabeled anti-CD4 and -CD8 cDbs.

Conclusion: These newly developed anti-CD4 and -CD8 immunoPET reagents represent a powerful resource to monitor T cell expansion, localization and novel engraftment protocols. Future potential applications of T cell targeted immunoPET include monitoring immune cell subsets in response to immunotherapy, autoimmunity, and lymphoproliferative disorders, contributing overall to preclinical immune cell monitoring.

KEY WORDS: ImmunoPET, $CD4^+$ and $CD8^+$ T cells, antibody fragments, hematopoietic stem cell transplant, Zirconium-89

INTRODUCTION

The ability to noninvasively monitor immune cells, specifically T cells, in the fields of oncology, immunotherapy, autoimmunity, and infection is difficult due to the complex nature of heterogeneous lymphocyte localization, proliferation and migration. Lymphocyte monitoring during immunotherapy protocols, such as detection of circulating lymphocytes from whole blood or tumor infiltrating lymphocytes from tissue biopsy, does not provide the full range of dynamic and spatial information needed. With the expanding implementation of immunotherapies, such as adoptive T cell transfer, hematopoietic stem cell or progenitor cell transfer, small molecule and antibody-based immunotherapies, and combinations thereof, whole body immuno-positron emission tomography (immunoPET) targeting of immune cell subtypes can potentially provide spatial and temporal information that is impossible utilizing current methods.

ImmunoPET takes advantage of the exquisite specificity and affinity of antibodies or antibody fragments and the sensitivity of PET (*1-3*). Intact antibodies have been engineered into bivalent antibody fragments such as the cys-diabody (cDb; dimer of scFv; Figure 1A) or minibody (Mb; dimer of scFv-C_H3) to enhance immunoPET imaging characteristics, including rapid clearance for high target-to-background images at short times post-injection, avidity, engineered sites for site-specific conjugation, and lack of Fc effector functions, among others (*4*).

Non-antibody based methods to detect lymphocytes using PET include direct cell labeling of cells ex vivo (*5-7*), reporter gene imaging of ex vivo genetically modified T cells (*8*), or the use of metabolic probes such as 2-deoxy-2-(^{18}F)fluoro-D-glucose ([^{18}F]-FDG), 3'deoxy-3'-(^{18}F)fluorothymidine ([^{18}F]-FLT), 1-(2'-deoxy-2'-

(^{18}F)fluoroarabinofuranosyl) cytosine ([^{18}F]-FAC), and 2'-deoxy-2'-(^{18}F)fluoro-9-β-arabinofuranosylguanine ([^{18}F]F-AraG) (*9-13*). Direct cell labeling suffers from limitations of radionuclide half-life, probe dilution due to cell division, and potential toxic effects due to the radiosensitivity of lymphocytes. Reporter gene tracking of T cells allows for longitudinal tracking, repeat monitoring and signal amplification due to cell division, but it requires the transfection of cells with exogenous DNA and the development of non-immunogenic reporters for translation (*14, 15*). The use of radiolabeled metabolic probes does not require ex vivo manipulation of cells but these probes are either not specific for T cells (e.g., [^{18}F]-FDG and [^{18}F]-FLT) or they target proliferating T cells in secondary lymphoid organs and fail to detect tumor-infiltrating lymphocytes (e.g., [^{18}F]-FAC).

Hematopoietic stem cell (HSC) therapy has become an attractive approach for the treatment of multiple malignancies (*16*). Currently many stem or progenitor cell therapies involving T cell receptor (TCR) or chimeric antigen receptor (CAR) targeting epitopes expressed on malignant cells are under development for clinical translation (*17-20*). Previous work utilizing PET to detect hematopoietic stem cell transfer and immune cell engraftment employs reporter genes to image total cell engraftment as opposed to lineage specific repopulation (*14, 21*). Here we report the development of anti-CD4 and -CD8 cDbs radiolabeled with ^{89}Zr for direct immunoPET detection of $CD4^+$ and $CD8^+$ T cells with the goal of detecting helper and cytotoxic lymphocyte repopulation after HSC therapy.

MATERIALS AND METHODS

C57BL/6, C57BL/6 SJL and AKR mice were obtained from the Jackson Laboratories and housed and maintained by the Department of Laboratory Animal Medicine at the University of California, Los Angeles. The UCLA Chancellor's Animal Research Committee approved protocols for all animal studies.

Detailed information regarding construction of anti-CD4 and -CD8 diabodies, protein expression and purification, flow cytometry, immunoPET, biodistribution and data analysis can be found in the supplemental materials.

Maleimide-DFO conjugation

The cDbs at 1-2.2 mg/mL were then reduced with 20-fold molar excess of tris(2-carboxyethyl)phosphine (TCEP; Pierce) for 30 min at room temperature. A 20-fold molar excess of N-(3,11,14,22,25,33-hexaoxo-4,10,15,21,26,32-hexaaaza-10,21,32-trihydroxytetratriacontane)malemide (malDFO; Macrocyclics) was then added and allowed to react for 2 h at room temperature. Excess malDFO was removed using PD-10 desalting columns (GE Healthcare) that were pre-equilibrated with PBS. Eluted protein was concentrated with Amicon Ultra centrifugal filters (0.5 mL and 10 kDa MWCO; Milipore). Conjugation efficiency was measured qualitatively by size exclusion chromatography using a Superdex 75 column on an AKTA purifier and SDS/PAGE-Coomassie stain analysis.

^{89}Zr radiolabeling

^{89}Zr-oxalate was obtained from Washington University School of Medicine, Division of Radiological Sciences, St. Louis Missouri or 3D Imaging LLC. Upon arrival, ^{89}Zr-oxalate was diluted with 40% (v/v) 2 M Na_2CO_3 and allowed to incubate for 3 min. The activity was then diluted with 2.5x volume of 1 M HEPES (pH 7.0). Final pH was checked with pHydrion plastic indicator strips (Micro Essential Laboratory) to confirm a pH of 7. MalDFO-conjugated protein was incubated for 1 h at room temperature at about 4-5 μCi/μg. Radiolabeling efficiency was measured by ITLC (Biodex Medical Systems) using 20 mM citrate buffer pH 5.6 as the mobile phase using a Wizard 3" 1480 Automatic Gamma Counter (Perkin-Elmer). Protein was purified using either BioRad6 Spin columns or PD-10 columns equilibrated with PBS. Radiochemical purity was assessed by ITLC as above.

Hematopoietic Stem Cell Transplant

150 mg/kg 5-fluorouracil (APP Pharmaceuticals) was injected i.v. into six- to ten-week old C57BL/6 SJL mice as previously described (*14*). Five days post-treatment, the bone marrow was harvested and cultured overnight with the following growth factors: stem cell factor (SCF; 100 ng/mL), IL-3 (6 ng/mL), IL-6 (10 ng/mL; all from Peprotech), and 5% (vol/vol) conditioned media from WeHi-3 cells (ATCC). 5 $x10^5$ HSCs were injected i.v. into eight week-old C57BL/6 mice that had been lethally irradiated (900 rad) on the same day.

RESULTS

Anti-CD4 GK1.5 Cys-Diabody Characterization

The anti-CD4 GK1.5 cDb was successfully engineered, produced, and purified with a final purified yield of 0.36 mg/L. The purity and molecular weight of the cDb were confirmed by SDS-PAGE and size exclusion chromatography (SEC; Figure 1B&C). Following mild reduction, GK1.5 cDb was conjugated to Alexa Fluor 488 C5-maleimide (mal488), with a recovery of 61% after purification. The conjugation resulted in a dye-to-protein molar ratio of 1.5:1 and the mal488 was bound to the monomeric protein as seen by SDS/PAGE analysis and fluorescent imaging of the gel (Figure 1B). Importantly, the elution profiles of the GK1.5 cDb and the mal488-GK1.5 cDb on SEC were similar (~55 kDa), demonstrating the conjugation to the Cys-tag has not disrupted the diabody conformation (Figure 1C). Mal488-GK1.5 cDb binds to primary cells isolated from the peripheral blood, thymus, spleen and lymph nodes of C57BL/6 (BL/6) mice similarly to the commercial GK1.5-APC-Cy7 antibody (Figure 1D).

Anti-CD4 GK1.5 Cys-Diabody Targets CD4$^+$ T Cells In Vivo

Conjugation of the GK1.5 cDb to maleimide-DFO (malDFO) did not alter the size exclusion profile of the DFO conjugated protein (Figure S1). The malDFO-GK1.5 cDb was radiolabeled with ^{89}Zr with a radiolabeling efficiency of 96.9 ± 1.5 % (range: 94 – 98%, n=5). After spin column purification, the radiochemical purity was >99.5% as shown by ITLC. The specific activity was 4.2 ± 1.6 μCi/μg (range: 1.6 – 5.5 μCi/μg, n=5).

Protein doses of 11.8 ± 1.4 μg (range: 10.3 – 14 μg, n=5) were injected intravenously via the tail vein into BL/6 mice. ImmunoPET acquisition at 4, 8 and 22 h post-injection showed a decrease in activity in the heart over time demonstrating blood clearance and radioactivity was detected with high contrast in various lymphoid organs and the kidney at 22 h post-injection (Figure 2A, top row). Targeting to the lymph nodes and spleen was confirmed by ex vivo biodistribution at 22 h post-injection (Figure 2B and Table S1). Interestingly, targeting to the thymus was not similar to other lymphoid organs.

In order to evaluate specificity, the ^{89}Zr-malDFO-GK1.5 cDb was injected into BL/6 mice that received either a bolus co-injection of 3 mg/kg non-radiolabeled GK1.5 cDb or anti-CD4 antibody depletion treatment. ImmunoPET of CD4-blocked and CD4-depleted mice shows more rapid clearance from the blood at 4 h post-injection and lower uptake in lymphatic organs when compared to wild type BL/6 mice (Figure 2A). Ex vivo biodistribution of CD4-blocked and CD4-depleted BL/6 mice confirmed a significant decrease in the lymph nodes, spleen, and thymus when compared to wild type BL/6 mice (Figure 2B and Table S1). Taken together these results confirm specific targeting of ^{89}Zr-malDFO-GK1.5 cDb to lymphoid organs.

Anti-CD8 2.43 Cys-Diabody Characterization

The previously engineered anti-CD8 2.43 minibody (*22*) was successfully re-engineered as a cDb and purified at high purity (Figure S2) with a yield of 2.44 mg/L. Superdex 75 SEC confirmed the correct molecular weight of ~55 kDa (Figure S2).

The 2.43 cDb was conjugated to mal488 with a recovery of 64% after purification with a dye-to-protein molar ratio of 0.9:1. The mal488 was covalently coupled to the monomeric 2.43 cDb as seen by fluorescence detection on SDS/PAGE (Figure S2) and the SEC elution profiles of the unconjugated 2.43 cDb and the mal488-2.43 cDb were very similar, confirming successful conjugation to the C-terminal cysteine of the diabody (Figure S2). The mal488-2.43 cDb retains antigen specificity for CD8α Lyt2.2$^+$ mouse strains (*22*) as demonstrated by flow cytometry analysis of primary cells isolated from the peripheral blood, thymus, spleen and lymph nodes (Figure 3).

Anti-CD8 2.43 Cys-Diabody Targets CD8$^+$ T Cells In Vivo

The 2.43 cDb was conjugated to malDFO (Figure S2) and radiolabeled with ^{89}Zr with a radiolabeling efficiency of 85.5 ± 12.5% (range: 66 - 97%, n=6) and the radiochemical purity was >99.4% as shown by ITLC. The specific activity was 3.4 ± 0.9 μCi/μg (range: 2.5 – 4.6 μCi/μg, n=6).

Protein doses of 10.9 ± 0.6 μg (range: 10 – 11.6 μg, n=6) ^{89}Zr-malDFO-2.43 cDb were injected intravenously into either wild type BL/6 mice (Figure 4A, top panel) or BL/6 mice that received a bolus co-injection of 3 mg/kg non-radiolabeled 2.43 cDb (Figure 4B, bottom panel). ImmunoPET images of ^{89}Zr-malDFO-2.43 cDb in wild type BL/6 show high background at 4 h post-injection that clears by 20 h for high contrast images. Ex vivo biodistribution of ^{89}Zr-malDFO-2.43 cDb acquired at 22 h post-injection in wild type and CD8-blocked BL/6 mice shows significantly less uptake in the spleen and lymph nodes, demonstrating CD8 specificity in vivo (Figure 4B and Table S2).

Targeting to the thymus of ^{89}Zr-malDFO-2.43 cDb was low and CD8-blocking does not decrease uptake.

T Cell Repopulation Post-Hematopoietic Stem Cell Transplant

BL/6 SJL ($CD45.2^+$) HSCs were intravenously injected into lethally irradiated BL/6 ($CD45.1^+$) mice to enable distinction between donor and host lymphocytes at two, four, and eight weeks post-HSC transplant using flow cytometry (Figure 5). At two weeks post-HSC transplant, the total donor cells were high in the peripheral blood and low in both the lymph nodes and spleen. By eight weeks, however, the donor cells are about 85% of the total $CD45^+$ cells in the lymph nodes, spleen, and peripheral blood, demonstrating efficient HSC engraftment and T cell repopulation.

When analyzing the $CD4^+$ T cell engraftment (Figure 5, middle row), the total CD4 numbers at two weeks post-HSC transplant were very low in the peripheral blood and spleen (about 5 and 3%, respectively) but high in the LNs (~40%) with the majority of the $CD4^+$ T cells being of host origin. At four weeks, the total $CD4^+$ T cells in the peripheral blood and spleen increased to about 12% with the majority of the $CD4^+$ T cells from donor origin. Interestingly, the total number of $CD4^+$ T cells in the LNs at four weeks decreased (~28%), but the percentage of donor $CD4^+$ T cells increased compared to the engraftment at two weeks post-HSC transplant. By eight weeks, the total $CD4^+$ T cells in the lymph nodes, peripheral blood and spleen were ~35, 22, and 18%, respectively, with the majority of $CD4^+$ T cells being of donor origin. Total CD8 cell numbers and repopulation of donor $CD8^+$ T cells at two, four and eight weeks post-HSC transplant (Figure 5, bottom row) were similar to that of CD4, but the total numbers of

$CD8^+$ T cells were about half of the total $CD4^+$ T cells. Thus, flow cytometry demonstrates effective repopulation of $CD4^+$ and $CD8^+$ T cells over time.

Anti-CD4 and -CD8 ImmunoPET Detection of T Cell Repopulation

^{89}Zr-malDFO-GK1.5 cDb and ^{89}Zr-malDFO-2.43 cDb were used to image $CD4^+$ and $CD8^+$ T cell reconstitution, respectively, in vivo at two, four and eight weeks post-HSC transplant (Figure 6 and Table S3). Detection of the lymph nodes from anti-CD4 and anti-CD8 immunoPET images in HSC transplanted mice increased from two to eight weeks post-HSC transplant. The biodistribution data of the anti-CD4 cDb, however, indicate that the %ID/g in the lymph nodes for the anti-CD4 repopulation was high at two and four weeks post-HSC transplant (axillary LNs: 75 ± 11 %ID/g and 79 ± 13 %ID/g, respectively) and decreased at eight weeks (39 ± 8.5 %ID/g). In the spleen, the %ID/g of ^{89}Zr-malDFO-GK1.5 cDb was moderate at two weeks post-HSC transplant (16 ± 2.0 %ID/g) and then increased at four and eight weeks post-HSC transplant (36 ± 3.4 %ID/g and 33 ± 3.1 %ID/g, respectively). The %ID/g for CD8 repopulation in both the spleen and the lymph nodes remained relatively constant from two to eight weeks post-HSC transplant (axillary LNs ranged from 18 – 20 %ID/g on average and spleen ranged from 17 – 28 %ID/g on average).

Representative computed tomography (CT) scans at two, four and eight weeks post-HSC transplant demonstrate a visible increase in size of the inguinal LN over time due to repopulation of the immune system (Figure S3). Inguinal LNs weighed 0.71 ± 0.12, 0.86 ± 0.20, and 2.0 ± 0.24 mg at two, four and eight weeks post-HSC transplant, respectively (Figure S3). These weights were used for estimating the total number of

cells, the total CD4$^+$ T cells, and total CD8$^+$ T cells at two, four and eight weeks post-HSC transplant (Figure S3). This indicates that not only do the percentages of donor T cells change as seen by flow cytometry, but the total number of lymphocytes also increased during repopulation and this is visualized by both anti-CD4 and -CD8 immunoPET.

DISCUSSION

By engineering the GK1.5 and 2.43 parental antibodies into cys-diabodies, we have developed immunoPET fragments for the detection of helper CD4$^+$ and cytotoxic CD8$^+$ T cells in vivo. Importantly, we have demonstrated that both the GK1.5 and 2.43 cDbs retain a true cross-paired diabody conformation following conjugation via the engineered C-terminal cysteine. It is important to verify maintenance of the proper conformation of cDbs as different linker lengths have the potential to induce higher molecular weight multimers (*23, 24*) or convert into monovalent scFvs following reduction and site-specific conjugation (*25*). Flow cytometry was used to demonstrate that the GK1.5 and 2.43 cDbs retain the ability to bind primary CD4$^+$ and CD8$^+$ T cells, respectively. Furthermore, we used microPET in wild type immunocompetent BL/6 mice in combination with antigen depletion and/or antigen blocking to demonstrate either CD4 or CD8 specificity in vivo and demonstrated the ability to monitor T cell repopulation post-HSC transplant.

Minibodies (~80 kDa) and cys-diabodies (~50 kDa) have different routes of clearance due to the renal filtration cutoff of ~60 kDa. The use of the residualizing radiometals, such as ^{64}Cu and ^{89}Zr, conjugated to minibodies or cys-diabodies causes

retention of radioactivity in the liver or kidney, respectively. Therefore, the high kidney uptake of both the ^{89}Zr-radiolabeled GK1.5 and 2.43 cys-diabodies is expected. The previously described ^{64}Cu-DOTA-2.43 minibody (*22*) suffered from aggregation problems leading to rapid clearance and high liver uptake but this allowed for high target-to-background images at only 4 hours post-injection. In the current work, the non-aggregating ^{89}Zr-malDFO-2.43 cDb demonstrated slower blood clearance than the respective 2.43 minibody and the improved time for imaging was 22 hours post-injection when the blood activity was 0.61 ± 0.06 %ID/g and inguinal LN:blood and spleen:blood ratios were 78:1 and 67:1, respectively. Previously, the 2.43 Mb derived from a CD8-depleting rat IgG2a antibody was shown to be non-depleting in vivo due to the lack of the complete Fc domain (*22*). The GK1.5 and 2.43 cDbs described in this work also lack the Fc domain and are expected to be non-depleting, which is critical in the development of immune cell targeting imaging agents.

An inherent problem of PET imaging of objects near or below the resolution of the PET scanner is the partial volume effect whereby the activity in a small organ is underestimated due to image reconstruction, attenuation, and positron path length prior to annihilation (*26*). Given the small animal scanner resolution of 1.4 mm FWHM (full width half maximal value), lymph nodes of about 1 mm in wild type mice, and the average positron path length of 1.1 mm for ^{89}Zr, a discrepancy exists between the %ID/g in lymph nodes obtained from PET imaging compared to the ex vivo biodistribution values. This discrepancy can be overcome by the use of partial volume correction to obtain accurate uptake values in small organs from PET images and our lab has derived recovery coefficients for both ^{89}Zr and ^{124}I using the Inveon microPET scanner (*27*).

Partial volume correction of lymph nodes, especially when reduced in size at two weeks post-HSC transplant, will suffer from error due to the small volume regions of interest where the recovery coefficient changes greatly for small changes in volume and the detectability of the lymph nodes.

Although detection of activity in lymph nodes is underestimated using PET, we successfully detected $CD4^+$ and $CD8^+$ T cell reconstitution at two, four, and eight weeks post-HSC transplant using the ^{89}Zr-malDFO-GK1.5 and ^{89}Zr-malDFO-2.43 cys-diabodies. Detection at 2 weeks post-HSC transplant proved more difficult as the lymph node size is small post-irradiation. We were able to detect $CD4^+$ T cells by immunoPET at 75 ± 11 %ID/g but not $CD8^+$ T cells at 20 ± 0.60 %ID/g in lymph nodes of the same size (0.74 ± 0.12 mg), demonstrating that if enough activity accumulates in a small organ, it is detectable by PET. The partial volume effect is also evident over the eight weeks post-HSC transplant using the anti-CD8 ^{89}Zr-malDFO-2.43 cDb. The ex vivo biodistributions of ^{89}Zr-malDFO-2.43 cDb at two, four and eight weeks post-HSC transplant in the lymph nodes are consistently around 20-25 %ID/g, but the corresponding immunoPET images show an increase of signal in the lymph nodes from two to eight weeks post-HSC transplant. This increased detection is due to the increased size of the lymph nodes over time resulting from immune cell repopulation. It should be noted that PET images of the HSC transplant model were scaled to the same %ID/g for consistent representation.

Interestingly, the thymus showed low uptake in wild type mice using anti-CD4 and -CD8 cDbs when compared to other T cell-rich lymphoid organs such as the lymph nodes and the spleen, limiting their use as thymic immunoPET imaging agents. The

parental anti-CD4 GK1.5 and anti-CD8 2.43 intact antibodies deplete CD4 or CD8 expressing cells in the thymus during antibody-based depletion therapy, so it is possible that the full Fc is required for efficient targeting to the thymus.

ImmunoPET and reporter genes provide different information in the context of TCR use in hematopoietic stem or progenitor cell therapy. Reporter genes allow for reporter probe uptake in the stem or progenitor cells primarily transduced and all successive cell types, such as T cells, B cells, monocytes, macrophages (*14*). Reporter genes provide an indication of total engraftment of donor cells but lack specificity for cell lineages. On the other hand, antibody-based immunoPET targeting lymphocytes provides an indication of CD4 or CD8 lymphocyte reconstitution, but cannot distinguish between host and donor lymphocytes. Imaging T cell expansion and localization, specifically tumor targeting, using lymphocyte-specific immunoPET could aid the monitoring of immunotherapeutic efficacy. In combination, reporter gene and CD4 and CD8 based immunoPET can provide information pertaining to the success of HSC transplant that was previously impossible.

CONCLUSION

Anti-CD4 and -CD8 immunoPET is a robust method for detection of lymphocytes in vivo and was shown to detect T cell repopulation in a model of syngeneic HSC transplantation. We believe immunoPET using radiolabeled antibody fragments specific for cell surface lineage markers will greatly aid the ability to monitor the dynamic nature of T cell subsets in models of disease and expand our knowledge of both T cells in vivo and immunotherapies.

ACKNOWLEDGEMENTS

We thank Dr. Waldemar Ladno, Darin Williams and Dr. David Stout at the UCLA Crump Institute for Molecular Imaging for help with microPET scans. We also thank Ralph and Marjorie Crump for a donation made to UCLA Crump Institute for Molecular Imaging.

REFERENCES

1. Wu AM, Senter PD. Arming antibodies: prospects and challenges for immunoconjugates. *Nat Biotechnol.* 2005;23:1137-1146.

2. Wu AM. Antibodies and antimatter: the resurgence of immuno-PET. *J Nucl Med.* 2009;50:2-5.

3. Knowles SM, Wu AM. Advances in immuno-positron emission tomography: antibodies for molecular imaging in oncology. *J Clin Oncol.* 2012;30:3884-3892.

4. Wu AM. Engineered antibodies for molecular imaging of cancer. *Methods.* 2014;65:139-147.

5. Matsui K, Wang Z, McCarthy TJ, Allen PM, Reichert DE. Quantitation and visualization of tumor-specific T cells in the secondary lymphoid organs during and after tumor elimination by PET. *Nucl Med Biol.* 2004;31:1021-1031.

6. Pittet MJ, Grimm J, Berger CR, et al. In vivo imaging of T cell delivery to tumors after adoptive transfer therapy. *Proc Natl Acad Sci U S A.* 2007;104:12457-12461.

7. Griessinger CM, Kehlbach R, Bukala D, et al. In vivo tracking of Th1 cells by PET reveals quantitative and temporal distribution and specific homing in lymphatic tissue. *J Nucl Med.* 2014;55:301-307.

8. Koya RC, Mok S, Comin-Anduix B, et al. Kinetic phases of distribution and tumor targeting by T cell receptor engineered lymphocytes inducing robust antitumor responses. *Proc Natl Acad Sci U S A.* 2010;107:14286-14291.

9. Aarntzen EH, Srinivas M, De Wilt JH, et al. Early identification of antigen-specific immune responses in vivo by [18F]-labeled 3'-fluoro-3'-deoxy-thymidine ([18F]FLT) PET imaging. *Proc Natl Acad Sci U S A.* 2011;108:18396-18399.

10. Nair-Gill E, Wiltzius SM, Wei XX, et al. PET probes for distinct metabolic pathways have different cell specificities during immune responses in mice. *J Clin Invest.* 2010;120:2005-2015.

11. Radu CG, Shu CJ, Nair-Gill E, et al. Molecular imaging of lymphoid organs and immune activation by positron emission tomography with a new [18F]-labeled 2'-deoxycytidine analog. *Nat Med.* 2008;14:783-788.

12. Ribas A, Benz MR, Allen-Auerbach MS, et al. Imaging of CTLA4 blockade-induced cell replication with (18)F-FLT PET in patients with advanced melanoma treated with tremelimumab. *J Nucl Med.* 2010;51:340-346.

13. Namavari M, Chang YF, Kusler B, Yaghoubi S, Mitchell BS, Gambhir SS. Synthesis of 2'-deoxy-2'-[18F]fluoro-9-beta-D-arabinofuranosylguanine: a novel agent for imaging T-cell activation with PET. *Mol Imaging Biol.* 2011;13:812-818.

14. McCracken MN, Gschweng EH, Nair-Gill E, et al. Long-term in vivo monitoring of mouse and human hematopoietic stem cell engraftment with a human positron emission tomography reporter gene. *Proc Natl Acad Sci U S A.* 2013;110:1857-1862.

15. Yaghoubi SS, Campbell DO, Radu CG, Czernin J. Positron emission tomography reporter genes and reporter probes: gene and cell therapy applications. *Theranostics.* 2012;2:374-391.

16. Wirth T, Parker N, Yla-Herttuala S. History of gene therapy. *Gene.* 2013;525:162-169.

17. De Oliveira SN, Ryan C, Giannoni F, et al. Modification of hematopoietic stem/progenitor cells with CD19-specific chimeric antigen receptors as a novel approach for cancer immunotherapy. *Hum Gene Ther.* 2013;24:824-839.

18. Vatakis DN, Arumugam B, Kim SG, Bristol G, Yang O, Zack JA. Introduction of exogenous T-cell receptors into human hematopoietic progenitors results in exclusion of endogenous T-cell receptor expression. *Mol Ther.* 2013;21:1055-1063.

19. Vatakis DN, Koya RC, Nixon CC, et al. Antitumor activity from antigen-specific CD8 T cells generated in vivo from genetically engineered human hematopoietic stem cells. *Proc Natl Acad Sci U S A.* 2011;108:E1408-1416.

20. Yang L, Baltimore D. Long-term in vivo provision of antigen-specific T cell immunity by programming hematopoietic stem cells. *Proc Natl Acad Sci U S A.* 2005;102:4518-4523.

21. Gschweng EH, McCracken MN, Kaufman ML, et al. HSV-sr39TK positron emission tomography and suicide gene elimination of human hematopoietic stem cells and their progeny in humanized mice. *Cancer Res.* 2014;74:5173-5183.

22. Tavaré R, McCracken MN, Zettlitz KA, et al. Engineered antibody fragments for immuno-PET imaging of endogenous CD8+ T cells in vivo. *Proc Natl Acad Sci U S A.* 2014;111:1108-1113.

23. Kortt AA, Lah M, Oddie GW, et al. Single-chain Fv fragments of anti-neuraminidase antibody NC10 containing five- and ten-residue linkers form dimers and with zero-residue linker a trimer. *Protein Eng.* 1997;10:423-433.

24. Kelly MP, Lee FT, Tahtis K, et al. Tumor targeting by a multivalent single-chain Fv (scFv) anti-Lewis Y antibody construct. *Cancer Biother Radio.* 2008;23:411-423.

25. Tavaré R, Wu WH, Zettlitz KA, et al. Enhanced immunoPET of ALCAM-positive colorectal carcinoma using site-specific 64Cu-DOTA conjugation. *Protein Eng Des Sel.* 2014;27:317-324.

26. Soret M, Bacharach SL, Buvat I. Partial-volume effect in PET tumor imaging. *J Nucl Med.* 2007;48:932-945.

27. Knowles SM, Zettlitz KA, Tavaré R, et al. Quantitative immunoPET of prostate cancer xenografts with 89Zr- and 124I-labeled anti-PSCA A11 minibody. *J Nucl Med.* 2014;55:452-459.

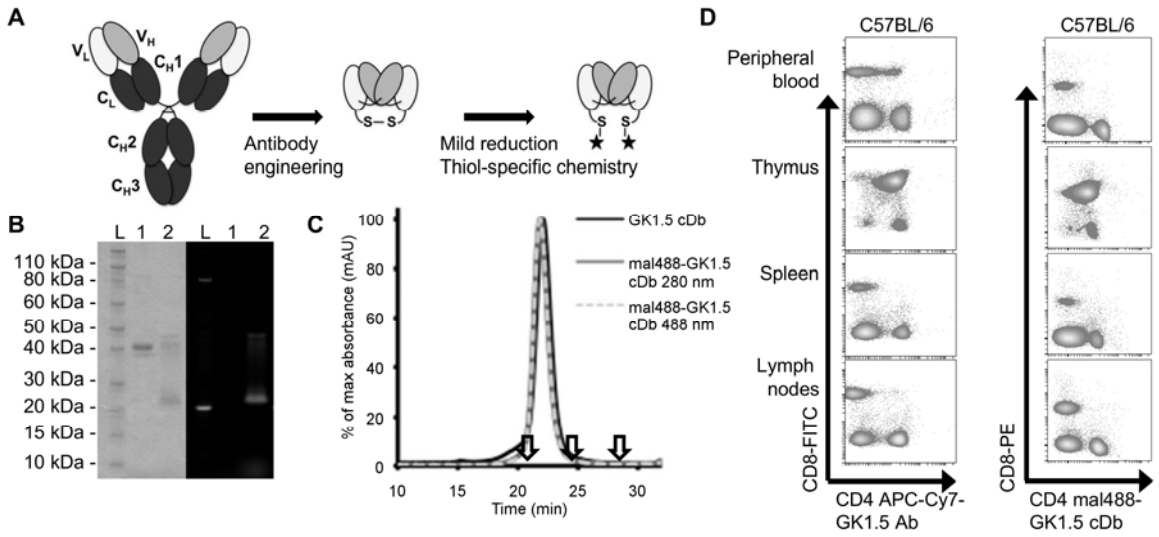

Figure 1. Anti-CD4 GK1.5 cDb characterization. (A) Schematic of intact antibody and engineered cys-diabodies for site-specific conjugation of fluorescent or metal chelator moieties via thiol-specific chemistry. **(B)** SDS/PAGE gel (left panel) of purified GK1.5 cDb (Lane 1) and mal488 conjugated GK1.5 cDb (Lane 2) for fluorescent flow cytometry binding assays. The UV image (right panel) of the same gel shows mal488 conjugated to GK1.5 cDb. **(C)** Size exclusion chromatography demonstrated the conjugation to mal488 did not disrupt the diabody conformation. Reference arrows indicate albumin (66 kDa) at 20.8 min, carbonic anhydrase (29 kDa) at 24.7 min, and cytochrome C (12.4 kDa) at 27.4 min. **(D)** Flow cytometry of single cell suspensions from the blood, thymus, spleen, and lymph nodes of C57BL/6 mice compares the binding of commercial anti-CD4-APC-Cy7 clone GK1.5 (left panel) and mal488-GK1.5 cDb (right panel).

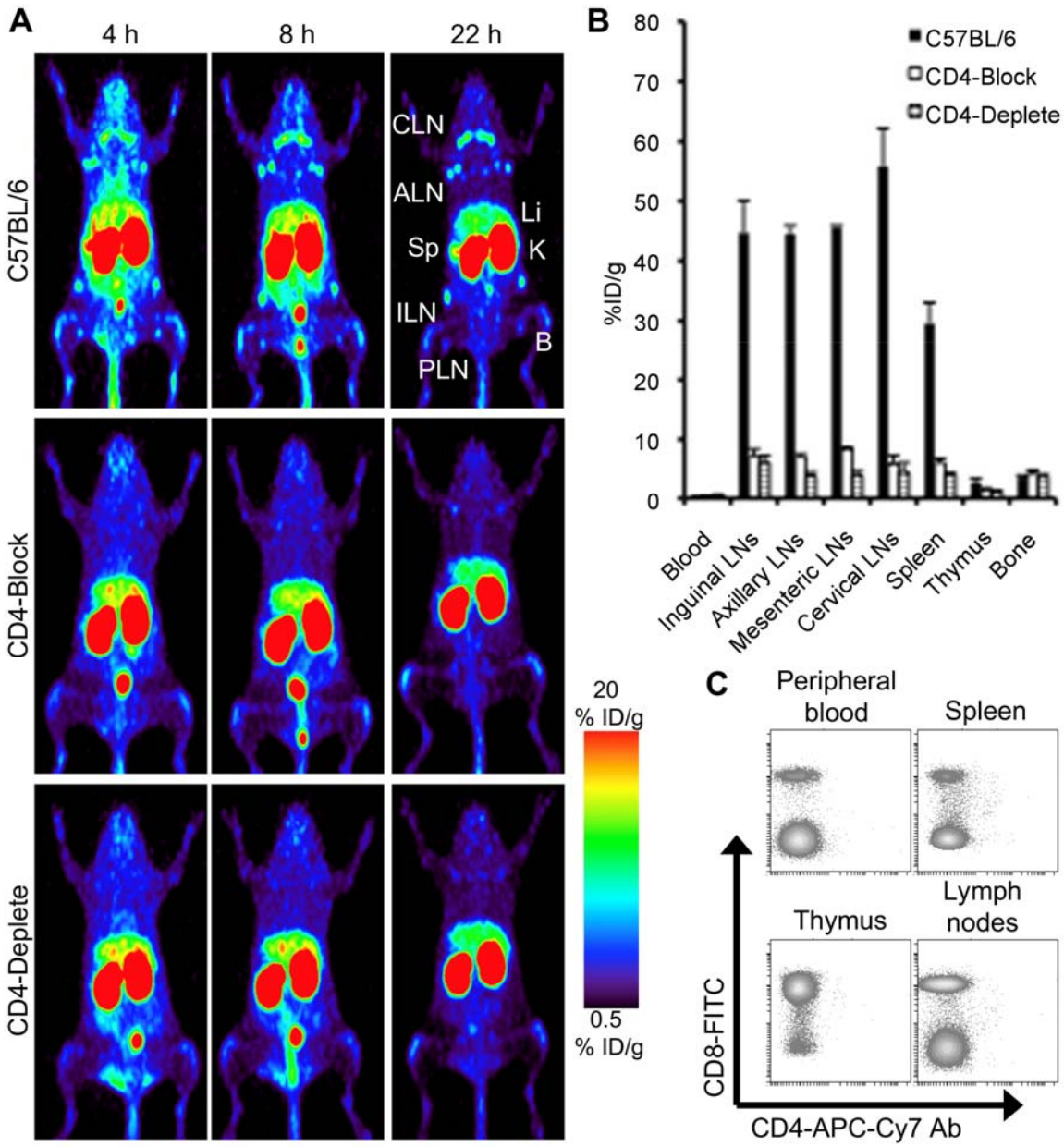

Figure 2. Anti-CD4 microPET of ^{89}Zr-malDFO-GK1.5 cDb in wild type, CD4-blocked and CD4-depleted C57BL/6 mice. (A) ^{89}Zr-malDFO-GK1.5 cDb was injected into wild type (top panel), CD4-blocked (bolus 3 mg/kg GK1.4 cDb; middle panel), and CD4-depleted (3 consecutive i.p. 25 mg/kg injections of GK1.5 Ab over 3 days; bottom panel) C57BL/6 mice and imaged at 4, 8, and 22 h post-injection. Images are represented as 25 mm MIPs. Abbreviations: CLN – cervical lymph node, ALN – axillary lymph

node, Li – liver, Sp – Spleen, K – Kidney, ILN – inguinal lymph node, B – bone, and PLN – popliteal lymph node. **(B)** Ex vivo biodistribution at 22 h post-injection of ^{89}Zr-malDFO-GK1.5 cDb from wild type, blocked and depleted C57BL/6 mice. (C) Flow cytometry of single cell suspensions from the blood, thymus, spleen, and lymph nodes of C57BL/6 mice treated with 3 consecutive i.p. 25 mg/kg injections of GK1.5 Ab over 3 days confirms the depletion of CD4 expressing cells.

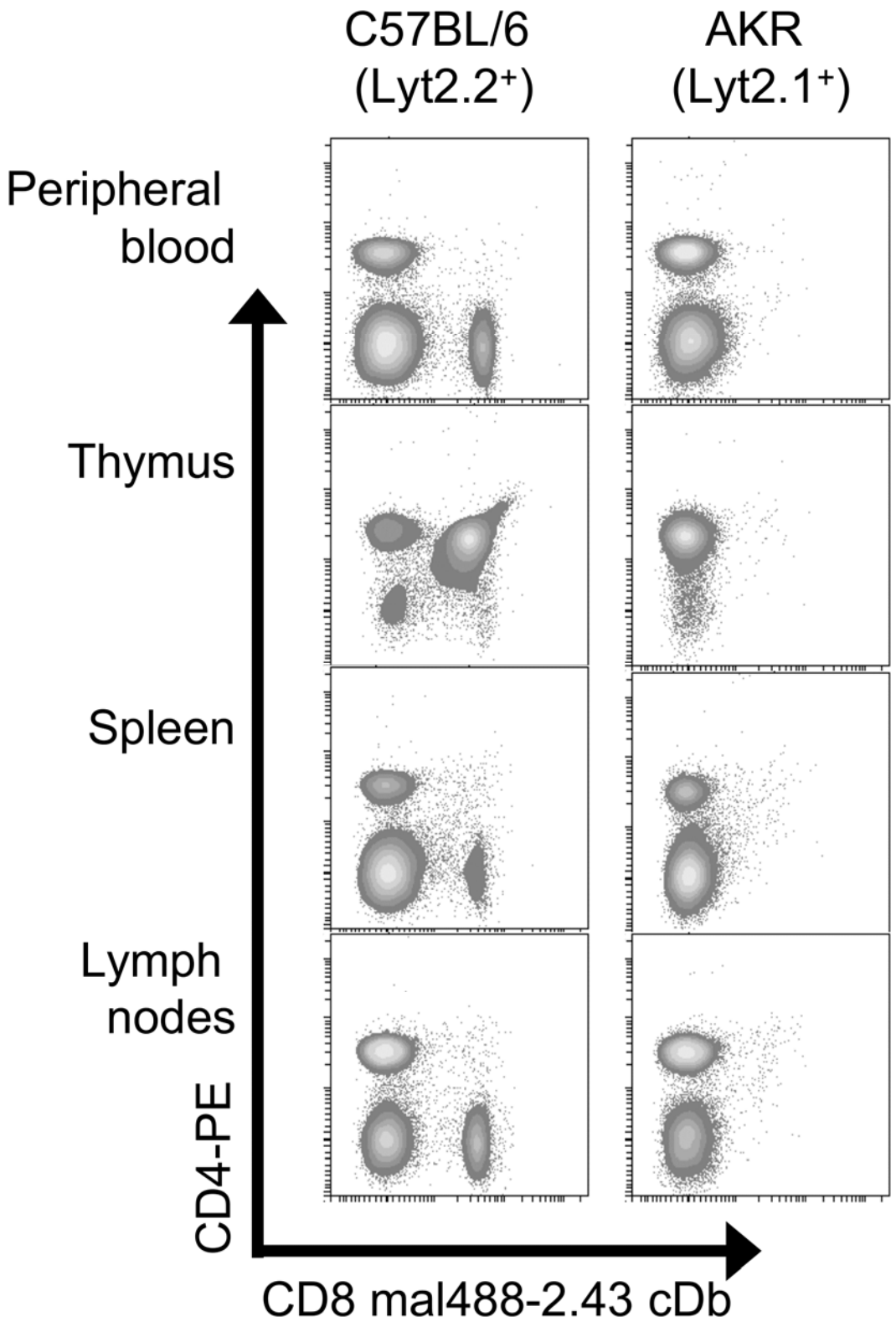

Figure 3. Engineered anti-CD8 2.43 cDb retains antigen specificity. Flow cytometry of single cell suspensions from the blood, thymus, spleen, and lymph nodes of Lyt2.2$^+$

C57BL/6 (left panel) and Lyt2.1$^+$ AKR mice (right panel) demonstrates that the mal488-2.43 cDb retains its antigen binding specificity.

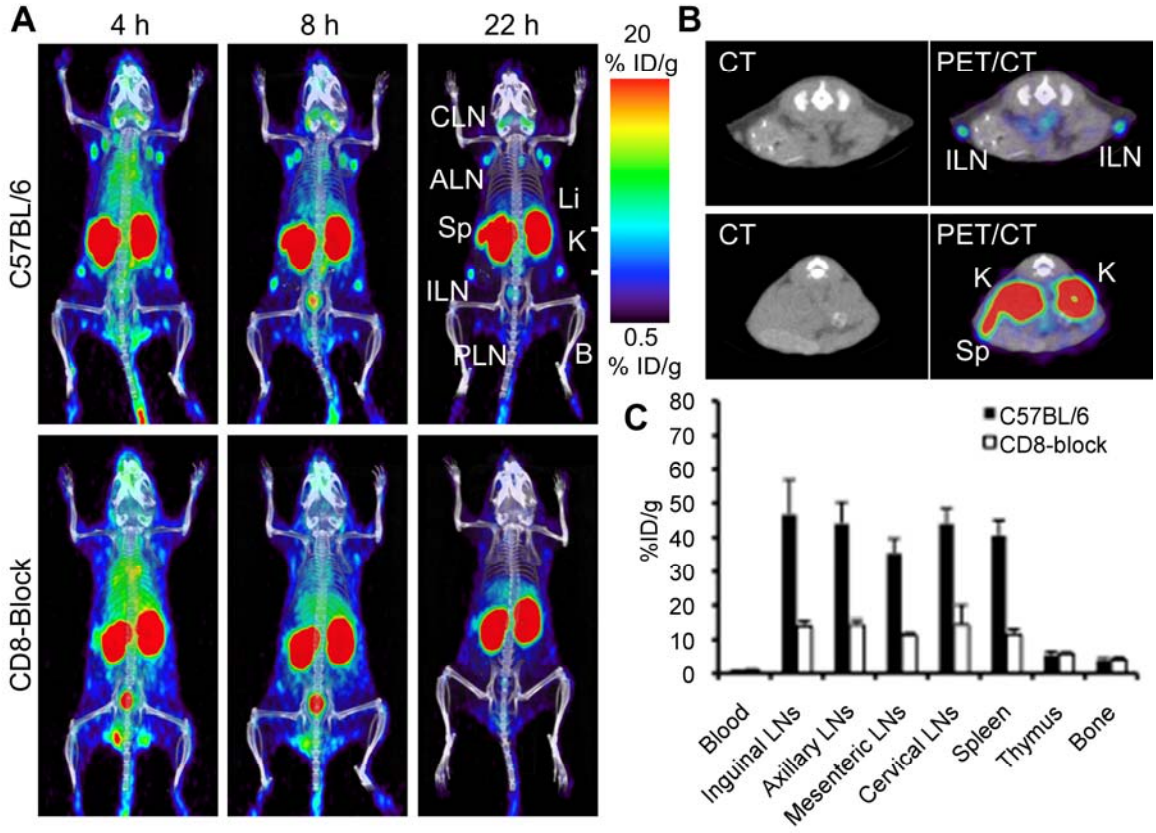

Figure 4. Anti-CD8 microPET/CT of ^{89}Zr-malDFO-2.43 cDb in wild type and CD8-blocked C57BL/6 mice. (A) ^{89}Zr-malDFO-2.43 cDb was injected into wild type (top panel) and CD8-blocked (bolus 3 mg/kg 2.43 cDb; bottom panel) C57BL/6 mice and imaged at 4, 8, and 22 h post-injection. Images are represented as coronal 25 mm MIPs. Abbreviations: CLN – cervical lymph node, ALN – axillary lymph node, Li – liver, Sp – Spleen, K – Kidney, ILN – inguinal lymph node, B – bone, and PLN – popliteal lymph node. **(B)** Transverse CT and PET/CT 0.5mm MIPs of the inguinal LNs (top panels) and spleen (bottom panels) in wt C57BL/6 mice at 22 h post-injection show PET coregistration with anatomical CT scans. Bars on coronal scan in top right panel of (A) indicate location of transverse images. **(C)** Ex vivo biodistribution at 22 h post-injection of ^{89}Zr-malDFO-2.43 cDb from wild type and blocked C57BL/6 mice.

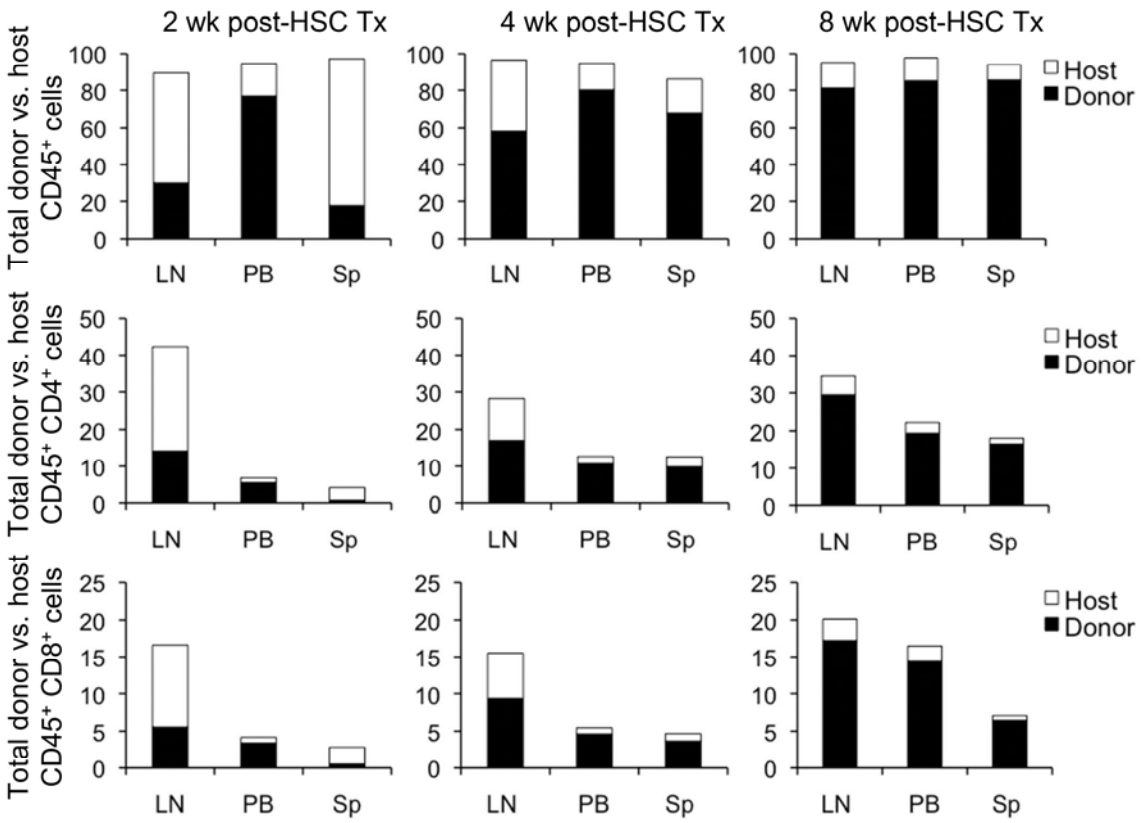

Figure 5. Flow cytometry analysis of CD4$^+$ and CD8$^+$ T cell reconstitution. Total donor versus host cells (top row), donor versus host CD4$^+$ T cells (middle row), and donor versus host CD8$^+$ T cells (bottom row) at two weeks (left column), four weeks (middle column), and eight weeks (right column) post-HSC transplant (n = 3 or 4). Single cell suspensions from the lymph nodes, peripheral blood, and spleen of mice are stained with anti-CD45.1 (donor), anti-CD45.2 (donor), anti-CD4, and anti-CD8 for flow cytometry analysis to quantify CD4$^+$ and CD8$^+$ T cell percentages.

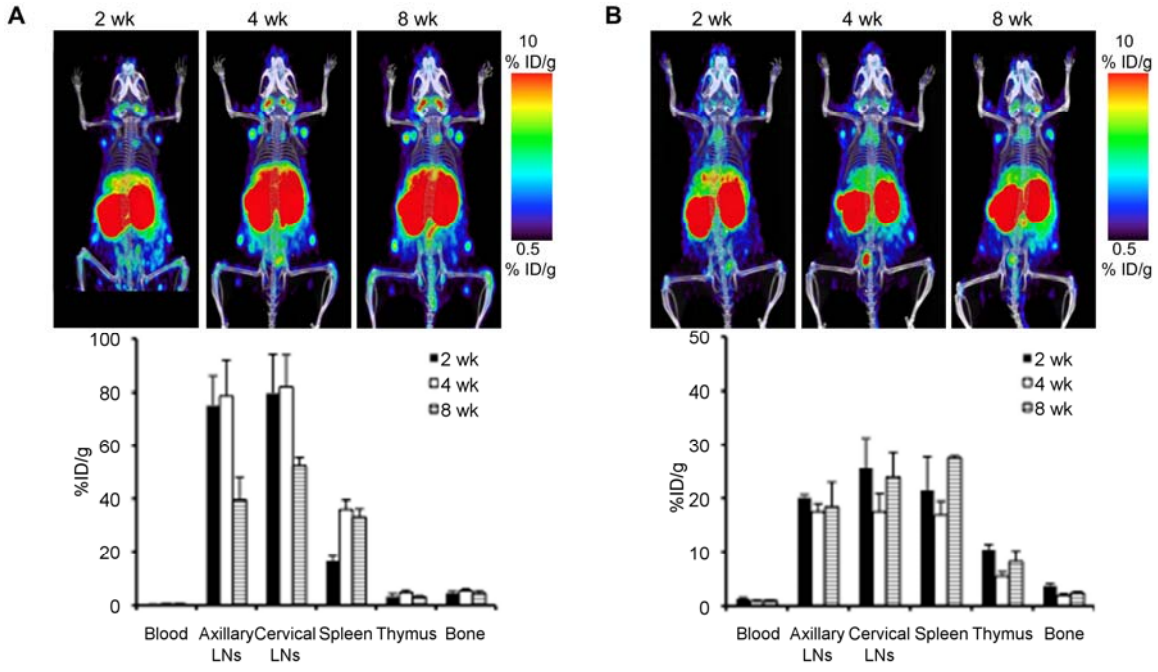

Figure 6. Anti-CD4 and -CD8 ^{89}Zr microPET/CT of T cell reconstitution post-HSC transplant. (A) ^{89}Zr-malDFO-GK1.5 cDb and **(B)** ^{89}Zr-malDFO-2.43 cDb were injected into C57BL/6 mice at 2, 4, and 8 weeks post-HSC transplant. ImmunoPET images were acquired at 22 h post-injection. Bottom panels are ex vivo biodistributions at 22 h post-injection.